ACS APPLIED MATERIALS & INTERFACES

www.acsami.org

Research Article

Effects of Valence States of Working Cations on the Electrochemical Performance of Sodium Vanadate

Wenchao Bi, Xiaodi Jiang, Chao Li, Yuan Liu, Guohua Gao,* Guangming Wu,* Muhammad Atif, Mohamad AlSalhi, and Guozhong Cao*

Cite This: *ACS Appl. Mater. Interfaces* 2022, 14, 19714–19724

Read Online

ACCESS | Metrics & More | Article Recommendations | Supporting Information

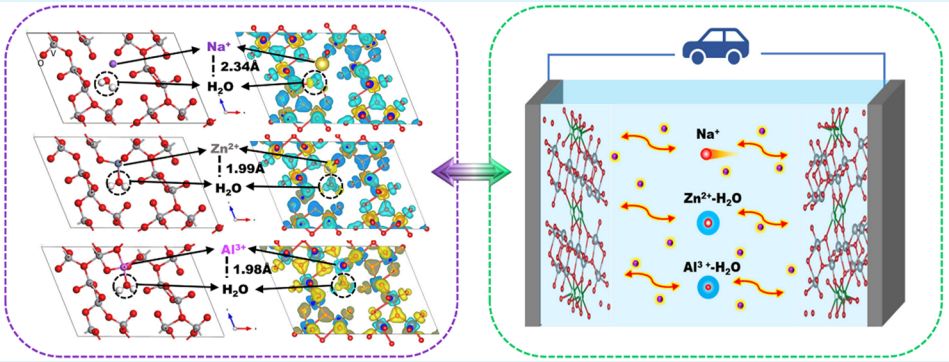

ABSTRACT: Supercapacitors have received much attention as large-scale energy storage devices for high power density and ultralong cycling life. In this work, sodium vanadate $Na_{0.76}V_6O_{15}$/poly(3,4-ethylenedioxythiophene) (PEDOT) nanocables with deficient bridge oxygen at the interface (denoted $Vo^{\bullet\bullet}$-PNVO) have been tailored for supercapacitors through the *in situ* polymerization of 3,4-ethylenedioxythiophene and studied using three different electrolytes. Experiments and theoretical calculations reveal that all Na^+, Zn^{2+}, and Al^{3+} ions appear as hydrates in aqueous solutions but insert into the crystal structure as Na^+ ions and Zn^{2+}-H_2O and Al^{3+}-H_2O hydrates, respectively. In comparison with the Zn^{2+}-H_2O and Al^{3+}-H_2O hydrates, Na^+ ions with a smaller radius diffuse more quickly in $Vo^{\bullet\bullet}$-PNVO. Thus, $Vo^{\bullet\bullet}$-PNVO delivers better charge storage capability and stability when an electrolyte with Na^+ ions is used. The results strongly suggest that an electrostatic interaction is significant in determining transport properties and storage capacities, rather than hydrate radii or valence states.

KEYWORDS: *electrostatic interaction, electrolyte cations, kinetics, sodium vanadate, supercapacitors*

1. INTRODUCTION

Energy storage technologies are indispensable for the application of intermittent renewable energy sources, including solar, hydro, and wind energy.[1,2] Supercapacitors have been applied in portable electronic products, electric vehicles, and many other fields, due to the advantages of short charging time, high power density, and ultralong cycling lifespan (>100000 cycles).[3,4] Supercapacitors are classified into electric double-layer capacitors (EDLCs) and pseudocapacitors according to the charge storage mechanism. EDLCs store charge by electrostatic absorption and desorption of opposite charges at the electrolyte surface layer. Pseudocapacitors rely on redox reactions between electrodes and the electrolyte.[5] In pseudocapacitors, also known as electrochemical capacitors, redox reactions happen at the electrode surface with electronic and ionic transportation inside the electrodes. The energy density of commercially available supercapacitors (~5 Wh kg^{-1}) is unsatisfactory in comparison with batteries (~200 Wh kg^{-1}).[3] Thus, more research efforts are underway to achieve excellent energy-storage capability without compromising the power density and charge and discharge stability of supercapacitors.

The electrochemical performance of supercapacitors relates to electrolytes due to their various physical and chemical properties, including different operating voltage, electrolyte ionic conductivity, and chemical stability.[2,4,6,7] Consequently, the specific capacitance and charge and discharge stability of a supercapacitor would be different. In terms of electrolytes, aqueous electrolytes prevail over organic electrolytes as well as ionic liquids because aqueous electrolytes are highly ion conductive (~1 S cm^{-1}), are simple to handle, have a low cost,

Received: February 16, 2022
Accepted: April 10, 2022
Published: April 20, 2022

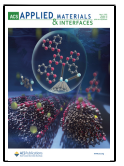

and are nonflammable.[6,8,9] In addition, supercapacitors with aqueous electrolytes achieve high power density due to a high ionic conductivity and dielectric constant and large surface area for small ions of the aqueous electrolyte. There are acidic (e.g., H_2SO_4[10]), alkaline (e.g., NaOH[11]), and neutral (e.g., Na_2SO_4[12]) aqueous solutions as electrolytes for supercapacitors. In fact, the electrolyte is chosen according to the electrode materials, which also greatly decides the storage capability of supercapacitors. For example, literally, the high redox activity of V_2O_5 species should be mainly in acidic solutions. However, on consideration of the safety issues and high price of corrosion-resistant current collectors by using acidic solutions, as well as the dissolution of V_2O_5 in aqueous alkali, neutral aqueous solutions are usually used as electrolytes for V_2O_5-based supercapacitors, where pseudocapacitive characteristics are also exhibited.[13,14] Moreover, it has been reported that hydrate radii of alkali-metal ions (Li^+, Na^+, and K^+) lead to different migration speeds and ion storage capabilities in MnO_2[8] and activated carbon.[15] However, for electrolytes with multivalent ions such as Zn^{2+} and Al^{3+}, it is necessary to explore whether the ionic radii, hydrate radii, or multivalent charge carriers would dominate the electrochemical performance of electrode materials.

Transition-metal oxides (e.g., MoO_3,[16] MnO_2,[17] and V_2O_5[18,19]) and conductive polymers (e.g., polypyrrole, polythiophene, and polyaniline)[20,21] are the main electrode materials for pseudocapacitors due to their high capacities from progressive redox reactions. Among these materials, V_2O_5 has been reported as a promising candidate for pseudocapacitors due to its layered structure for high theoretical capacitance (~2120 F g^{-1}), proper voltage window, and abundant resource.[5] Recent progress has shown that a nanostructure helps to enlarge the surface area of pure V_2O_5 and its derivatives, but the electrochemical performance is less satisfactory (180.7 F g^{-1} for a $V_2O_5{\cdot}0.6H_2O$ nanoribbon[14]) because of poor conductivity and structure instability. Compositing with conductive materials can help to enhance the capacity and cycling stability of V_2O_5: for instance, compositing V_2O_5 with graphene and CNT, conductive polyaniline,[13] and so on. Defect engineering, such as oxygen vacancies, can also effectively enhance the electrochemical properties of electrode materials with enhanced charge storage kinetics.[16,22,23] Our previous studies found that introducing oxygen vacancies would effectively facilitate charge transfer and enhance the ion diffusion kinetics of V_2O_5 nanofibers with an enlarged lattice space for supercapacitors.[24] Moreover, the cycling stability of V_2O_5/polyaniline is synergistically improved by oxygen vacancies and the polyaniline coating (110% capacitance retention over 20000 charge/discharge processes).[24] In addition to the above achievements of oxygen vacancies in layered V_2O_5, oxygen vacancies in V_2O_5 derivatives with different crystalline structures also affect the charge kinetics of electrodes. For instance, in tunnel-structured $Na_{0.76}V_6O_{15}$, oxygen vacancies and conductive polymers synergistically promoted the Zn^{2+} intercalation/deintercalation for zinc ion batteries.[25] However, the related studies on supercapacitors are insufficient. They are significant and necessary for supercapacitor applications, especially in exploring the effects of various aqueous electrolytes on supercapacitors.

In our study, oxygen vacancies ($Vo^{\bullet\bullet}$) contained in sodium vanadate nanocables ($Na_{0.76}V_6O_{15}$/poly(3,4-ethylenedioxythiophene, denoted $Vo^{\bullet\bullet}$-PNVO) were prepared and optimized with temperature as the electrode materials of supercapacitors. The effects of ionic radius, hydrate radius, valence states, and electrostatic interactions of working cations (including Na^+, Zn^{2+}, and Al^{3+}) on the charge storage capabilities were explored. The related kinetic properties were analyzed by theoretical calculations with bond changes and charge density distributions and further confirmed by experimental data.

2. EXPERIMENTAL SECTION

2.1. Synthesis of $Na_{0.76}V_6O_{15}$/PEDOT Nanocables ($Vo^{\bullet\bullet}$-PNVO). $Vo^{\bullet\bullet}$-PNVO was synthesized with our reported method.[25] V_2O_5 powder (0.5 g) was added to deionized water (50 mL) and the mixture stirred for 2 h. Next, 30 mL of a deionized water solution of sodium dodecyl benzenesulfonate (1.0 g) was added and the mixture stirred for 2 h. This mixture was transferred to a 100 mL Teflon-lined stainless-steel autoclave and kept at 180 °C for 7 days. Deionized water and ethanol were used for solvent replacement, following with freeze-drying under vacuum and annealing at 450 °C in air for 3 h. Then, the obtained NVO was treated with 0.5 mL of HCl under vacuum at room temperature for 1 h. After that, the sample was placed to a vacuum reactor containing 0.1 mL of 3,4-ethylenedioxythiophene (EDOT) at 25, 50, and 80 °C for 8 h, respectively. $Vo^{\bullet\bullet}$-PNVO nanocables were obtained after further drying in air at 120 °C overnight.

2.2. Material Characterizations. X-ray diffraction (XRD) measurements were performed with a Bruker D8 Discover X-ray diffractometer and an ImS 2-D detection system (50 kV, 1000 mA). Fourier-transform infrared (FTIR) with a Bruker-TENSOR27 instrument, Raman with a Jobin-Yvon HR800 microscope (λ = 514 nm), and thermogravimetric and differential scanning calorimetry (TG-DSC) with an SDT Q600 instrument (10 °C min^{-1}, flowing air). Electron spin resonance (ESR) was carried out on a Bruker BioSpin instrument. X-ray photoelectron spectra (XPS) were obtained with a a Thermo ESCALAB 250XiX spectrometer in the PHI-5,000C ESCA system with Mg Kα radiation ($h\nu$ = 1253.6 eV). A field-emission scanning electron microscope (FE-SEM; S-4800) and a high-resolution transmission electron microscope (HRTEM; JEOL-JEM2100) were used.

2.3. Electrochemical Measurements. The electrodes were prepared first. The active materials, acetylene black and poly(vinylidene fluoride) in *N*-methylpyrrolidone, were mixed with a mass ratio of 8:1:1. This slurry was painted onto a graphite paper current collector and dried under vacuum at 100 °C overnight. Electrodes were tested with symmetrical electrode systems in three different electrolytes, including 0.5 M Na_2SO_4, 1 M $ZnSO_4$, and 0.5 M $Al_2(SO_4)_3$ solutions. The specific capacitance of an electrode (C, F g^{-1}) is calculated from the discharge curves according to $C = 2I\Delta t/(m\Delta V)$, where I, m, Δt and ΔV are the constant discharge current, total loading mass, discharge duration, and voltage window of each electrode, respectively. Energy density (E, W h kg^{-1}) and power density (P, W kg^{-1}) were calculated with the equations $E = (1/8)C(\Delta V)^2/3600$ and $P = E/\Delta t$, respectively.

2.4. Density Functional Theory (DFT) Calculations. The Vienna *ab initio* simulation package (VASP)[26] was used in these calculations. The Perdew–Burke–Ernzerhof variant of the generalized gradient approximation (GGA) was chosen to treat the exchange and correlation energy functional.[27] The projector augmented wave pseudopotential approach (PAW) was used to the describe interaction between ions and electrons;[28,29] the energy cutoff for the plane wave basis was set to 500 eV, and the total energy was converged to 10^{-5} eV. The electronic structure of vanadium was described with effective U parameters of 3.1 eV.[30] The lattice parameters of $M_{0.76}V_6O_{15}$, where M denotes Na, Zn, and Al, were set to be 15.85 Å × 3.68 × 10.41 Å with α = 90°, β = 112°, and γ = 90°.

3. RESULTS AND DISCUSSION

3.1. Characterization of $Vo^{\bullet\bullet}$-PNVO and NVO. $Vo^{\bullet\bullet}$-PNVO was obtained when vapor EDOT deposited, oxidatively

https://doi.org/10.1021/acsami.2c02920
ACS Appl. Mater. Interfaces 2022, 14, 19714−19724

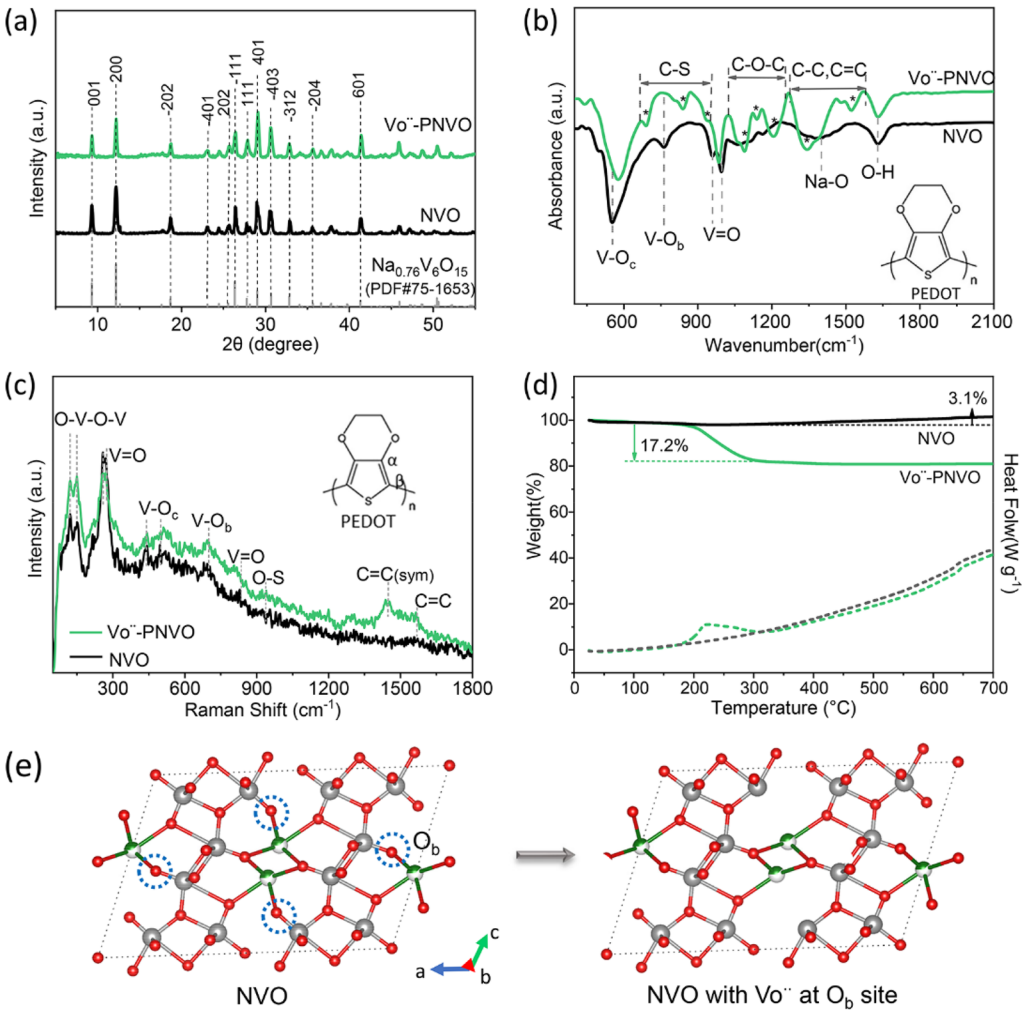

Figure 1. (a) XRD patterns, (b) FTIR spectra, (c) Raman spectra, and (d) TG-DSC curves of $Vo^{\bullet\bullet}$-PNVO and NVO. (e) Crystal structures of NVO and NVO with oxygen vacancies ($Vo^{\bullet\bullet}$) at the O_b site.

polymerized *in situ* on the surface of NVO at 80 °C,[25] and formed oxygen vacancies simultaneously in the surface layer of NVO. The oxidative polymerization of EDOT monomers related to electron loss and deprotonation[31] can be described as follows:

$$nC_6H_6O_2S - (2n-2)e' \rightarrow H(C_6H_4O_2S)_nH + (2n-2)H^+ \quad (1)$$

As $Vo^{\bullet\bullet}$ and O'' are generated in the NVO primitive lattice when electrons in oxygen (O_o^x) are lost, O'' and H^+ would form H_2O and V_v' and V_v'' would form when V_v^x receives the above electrons:

$$O_o^x = Vo^{\bullet\bullet} + O'' + e' \quad (2)$$

$$2H^+ + O'' \rightarrow H_2O(g) \quad (3)$$

$$V_v^x + e' \rightarrow V_v' \quad V_v' + e' \rightarrow V_v'' \quad (4)$$

Reactions 1−4 are summarized as

$$nC_6H_6O_2S + 2(n-1)V_v^x + (n-1)O_o^x \rightarrow H(C_6H_4O_2S)_nH + mV_v' + \left(n-1-\frac{1}{2}m\right)V_v'' + (n-1)Vo^{\bullet\bullet} + (n-1)H_2O(g) \quad (5)$$

where n and m are random variable parameters.

In Figure 1a, XRD patterns display a crystalline phase of $Na_{0.76}V_6O_{15}$ (JPDS No.75-1653) in both $Vo^{\bullet\bullet}$-PNVO and NVO. In this tunnel structure, $[V_6O_{15}]_n$ layers are connected by VO_6 octahedra with oxygen atoms (Figure 1e). The relatively weak intensity of $Vo^{\bullet\bullet}$-PNVO peaks indicates that $Vo^{\bullet\bullet}$-PNVO is amorphous, probably caused by PEDOT and/or oxygen vacancies.

In the FTIR spectra (Figure 1b), NVO displays the stretching vibration modes of a V−O_c bond (493, 553 cm^{-1}), a V−O_b bond (767 cm^{-1}), a terminal V═O bond (958, 995 cm^{-1}), an Na−O bond (1377 cm^{-1}), and an O−H bond of absorbed water (1631 cm^{-1}).[32,33]

In $Vo^{\bullet\bullet}$-PNVO, the existence of PEDOT is confirmed by a C−S bond (690, 839, 933 cm^{-1}), a C−O−C bond (1087, 1140, 1207 cm^{-1}), and C−C and C═C bonds (1397, 1522 cm^{-1}).[34] Moreover, the V−O_c bond becomes stronger with an obvious blue-shifted peak, the V−O_b peak disappears, and the V═O bond (984 cm^{-1}) only appears as one peak.[32] These

https://doi.org/10.1021/acsami.2c02920
ACS Appl. Mater. Interfaces 2022, 14, 19714−19724

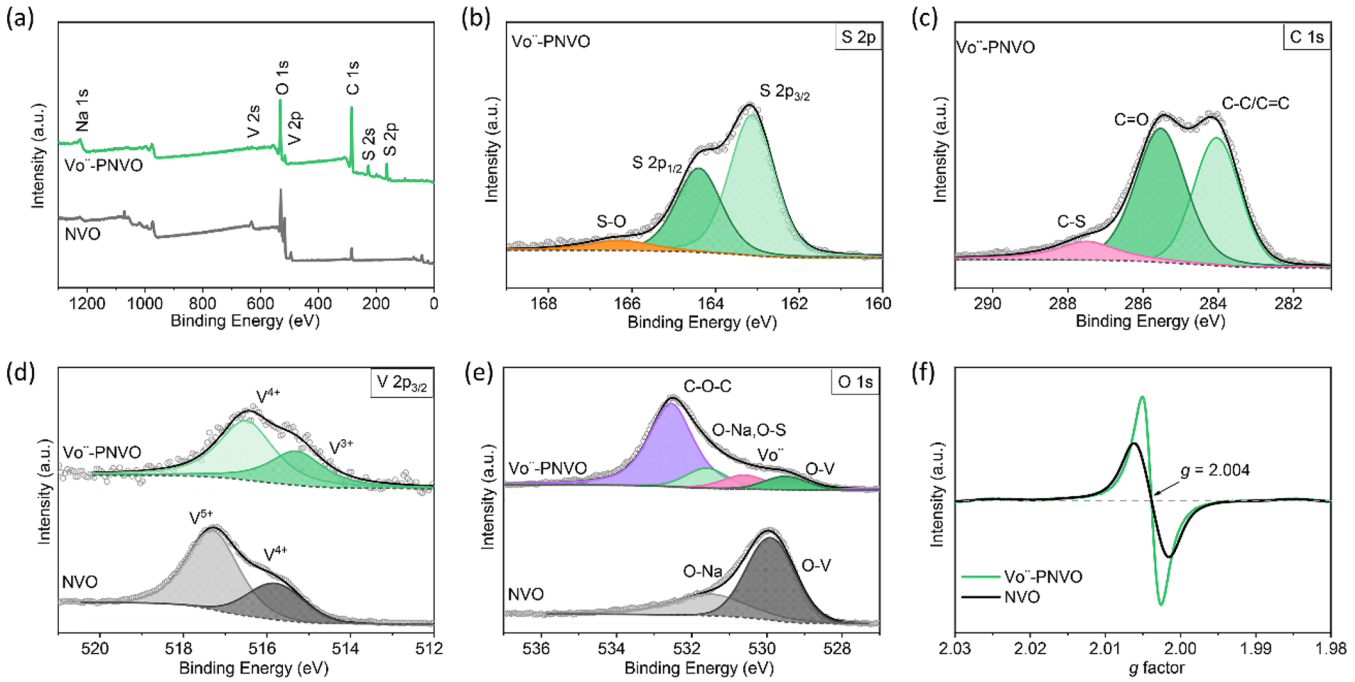

Figure 2. XPS analysis of Vo••-PNVO and NVO: (a) full survey; (b) S 2p; (c) C 1s; (d) V $2p_{3/2}$; (e) O 1s. (f) ESR results of Vo••-PNVO and NVO.

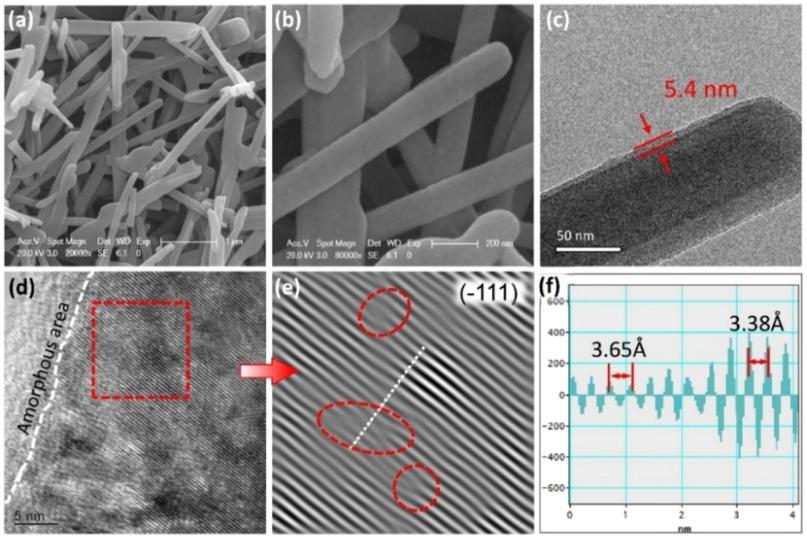

Figure 3. (a, b) SEM, (c) TEM, and (d) HRTEM images of Vo••-PNVO and (e) the corresponding IFFT image and (f) line profile of the dashed line in (e).

changes should be ascribed to oxygen vacancies and connections between PEDOT and NVO,[35] which will be further discussed next.

In Raman spectra (Figure 1c), the weak peaks for the O−V−O−V bond suggest a reduced compressive deformation of the lattice[32,36] and a larger lattice space for ion diffusion in Vo••-PNVO (also evidenced by IFFT images). The weak peaks of V═O bonds at 258 and 265 cm^{-1} show a red shift of 28 cm^{-1} due to the O−S connections between NVO and PEDOT.[35] A blue shift in the V−O_c bond at 516 cm^{-1} is in accord with an FTIR analysis.[37] The V−O_b bond becomes weak with a blue shift to 695 cm^{-1},[38,39] while there are no peaks in FTIR spectra. This is explained by partial V−O_b bonds at the interface being weakened by oxygen vacancies and the NVO crystalline structure inside remaining unchanged, in accordance with our reported Vo••-V_2O_5/polyaniline.[24] PEDOT is confirmed by symmetrical and asymmetrical C═C at 1453 and 1560 cm^{-1}.[37,40,41] On the basis of the above FTIR and Raman analysis, PEDOT connects NVO with terminal oxygen, forming oxygen vacancies at the O_b site. Consequently, an enlarged channel would provide for ion diffusion, as shown in Figure 1e. In TG-DSC curves (Figure 1d), the mass of PEDOT in Vo••-PNVO is about 17.2%.[42]

In XPS spectra in Figure 2a, a signal of S element from PEDOT is detected in Vo••-PNVO. The S 2p spectrum is deconvoluted into S $2p_{3/2}$, S $2p_{1/2}$ and S−O (Figure 2b).[34,43] In Figure 2c, C−C/C═C, C−S, and C = O belonging to PEDOT can be seen in the C 1s spectrum of Vo••-

https://doi.org/10.1021/acsami.2c02920
ACS Appl. Mater. Interfaces 2022, 14, 19714−19724

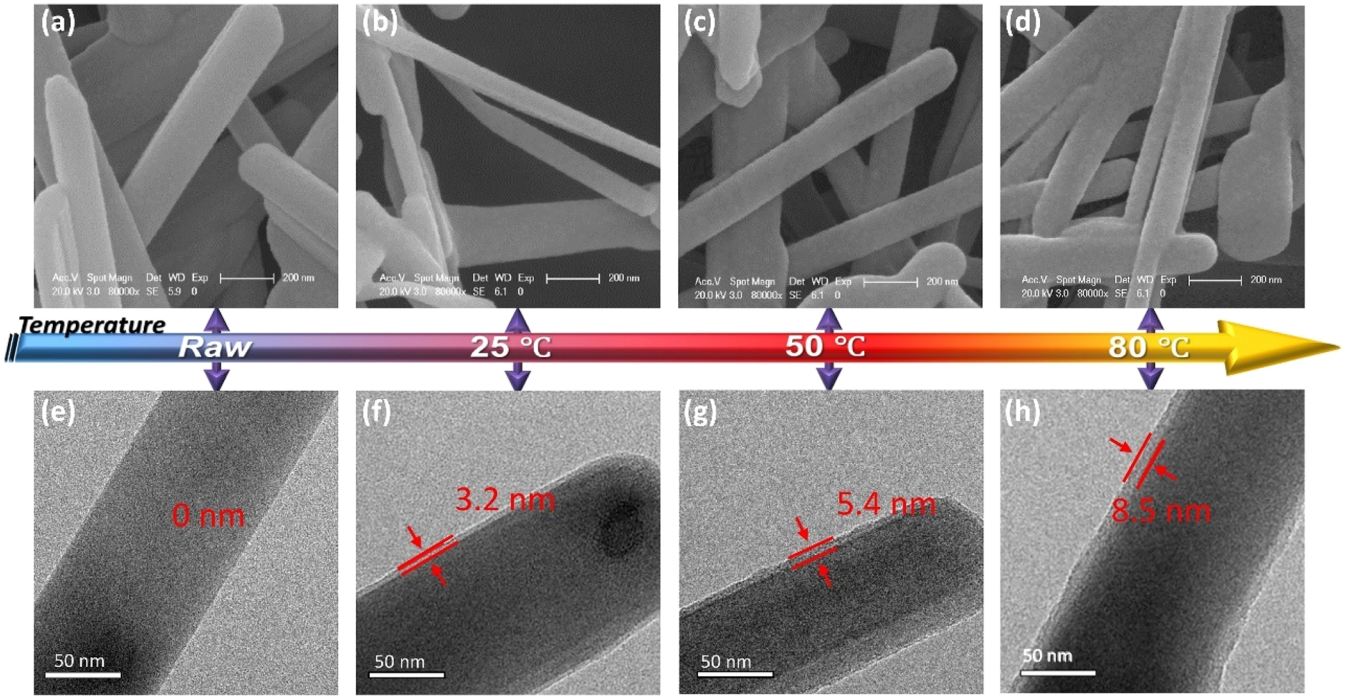

Figure 4. (a–d) SEM and (e–h) TEM images of $Vo^{\bullet\bullet}$-PNVO synthesized at different temperatures.

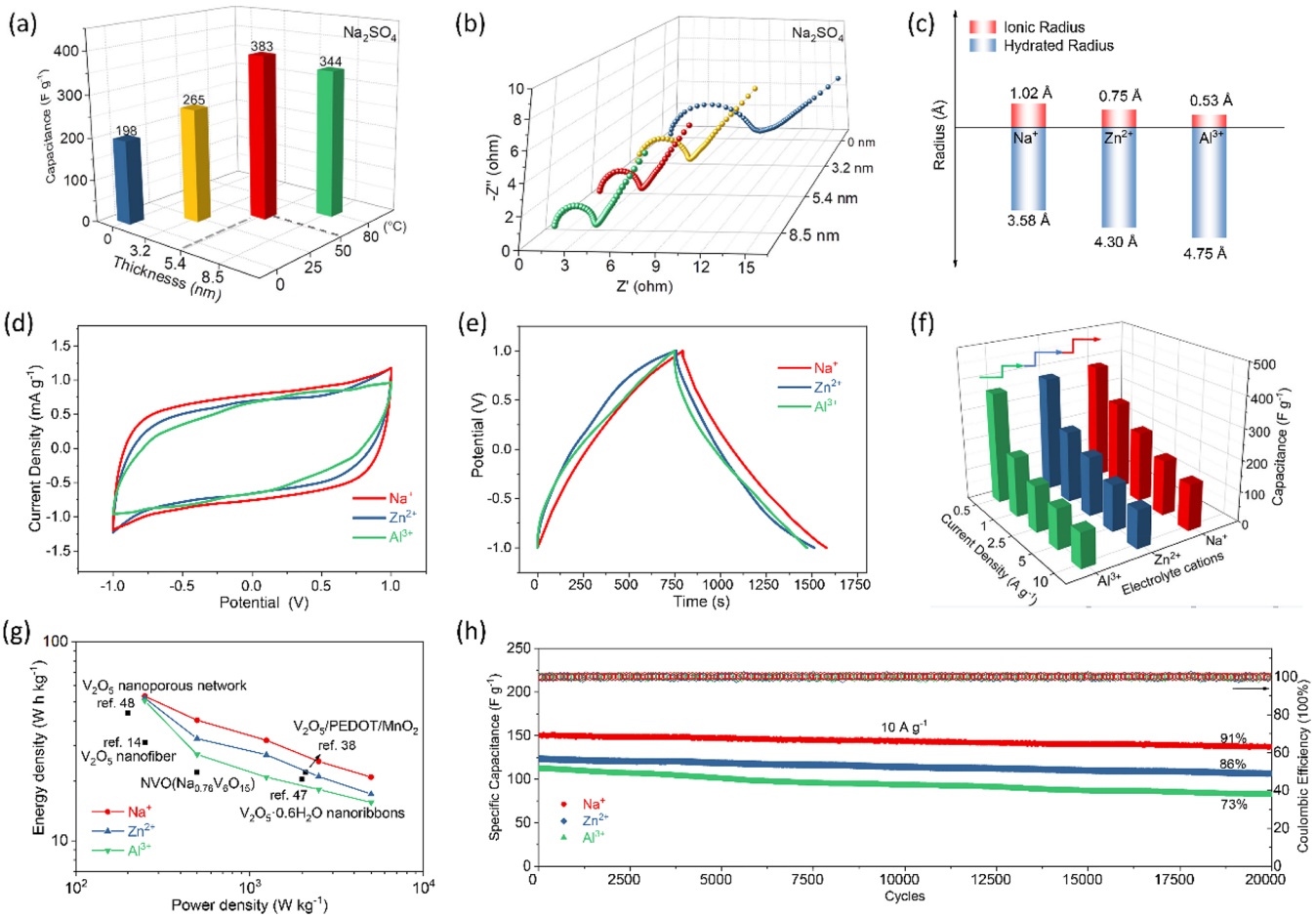

Figure 5. (a) Relationship among the specific capacitance (0.5 A g^{-1}), polymerization temperature, and PEDOT coating thickness of $Vo^{\bullet\bullet}$-PNVO. (b) EIS curves of different $Vo^{\bullet\bullet}$-PNVO samples. (c) The reported ionic radii and hydrate radii of Na^+, Zn^{2+}, and Al^{3+}.[50] (d) CV curves (5 mV s^{-1}), (e) GCD curves (0.5 A g^{-1}), (f) specific capacitance, (g) Ragone plots, and (h) cycling performance of $Vo^{\bullet\bullet}$-PNVO in different electrolytes.

https://doi.org/10.1021/acsami.2c02920
ACS Appl. Mater. Interfaces 2022, 14, 19714–19724

PNVO.[34,37,44] In Figure 2d, the asymmetric V $2p_{3/2}$ spectrum is divided into V^{5+} (517.3 eV) and V^{4+} (515.9 eV) in NVO, while it is divided into V^{4+} (516.6 eV) and V^{3+} (515.3 eV) peak in $Vo^{\bullet\bullet}$-PNVO. This suggests that some V^{5+} and V^{4+} ions are reduced due to oxygen vacancies.[24] Oxygen vacancies are further confirmed by the O 1s spectra in Figure 3e. For O 1s spectra, O−V (529.6 eV), oxygen vacancies (530.5 eV), O−Na/O−S (531.5 eV) and C−O from PEDOT (532.8 eV) are shown in $Vo^{\bullet\bullet}$-PNVO,[38,45,46] while only O−V (529.9 eV) and O−Na (531.4 eV) appear in NVO.[38]

EPR bulk measurements were conducted to examine oxygen vacancies after the surface characterizations of XPS. Unpaired electrons can be identified by EPR, including oxygen vacancies and V^{4+}.[47] In Figure 2f, the two samples exhibit typical a EPR response at g = 2.004 and $Vo^{\bullet\bullet}$-PNVO has a stronger peak in comparison to NVO This is because oxygen vacancies and V^{4+} are generated, although some V^{4+} simultaneously turns into V^{3+} in $Vo^{\bullet\bullet}$-PNVO.[37,38,47] In nanocable-structured $Vo^{\bullet\bullet}$-PNVO, the slight difference in bulk EPR characterization and significant changes by surface XPS characterization suggest oxygen vacancies are distributed at the interface in $Vo^{\bullet\bullet}$-PNVO.[25,35]

In SEM and TEM images (Figure 3a−c), $Vo^{\bullet\bullet}$-PNVO exhibits a nanocable structure and the coating thickness is ∼5.4 nm. The coating uniformity is examined by TEM-EDS in Figure S1, where the S element is distributed homogeneously and more broadly. In the HRTEM image (Figure 3d), the amorphous interface between PEDOT and NVO indicates that oxygen vacancies are introduced in the surface layer of NVO. In the corresponding IFFT image of $Vo^{\bullet\bullet}$-PNVO (Figure 3e), dislocations are found (red circles), and the (−111) plane shows an expanded interplanar space of 3.65 Å (Figure 3f). As oxygen vacancies cause the surrounding atoms to be skewed and dislocated, the interplanar space is expanded. Moreover, the accompanying V^{4+}, which is larger (72 pm) than V^{5+} (68 pm), may also enlarge the interplanar distance. Note that there is no peak shift in XRD patterns because the inner crystalline structure is not changed by interface-located oxygen vacancies. Thus, there would be more space available for faster ion diffusions in $Vo^{\bullet\bullet}$-PNVO when oxygen vacancies are generated.

3.2. Electrochemical Characterizations of Optimized $Vo^{\bullet\bullet}$-PNVO. In this section, the electrochemical properties of $Vo^{\bullet\bullet}$-PNVO in different electrolytes are explored. On consideration that both oxygen vacancies and PEDOT thickness can affect the electrochemical properties of electrodes[12] and oxygen vacancies are induced by PEDOT polymerization, the PEDOT thicknesses (oxygen vacancies) of $Vo^{\bullet\bullet}$-PNVO were first optimized by different polymerization temperatures. XRD patterns (Figure S2) indicate that all samples keep the crystalline phase unchanged. As shown in SEM and TEM images (Figure 4a−h), the PEDOT thickness of $Vo^{\bullet\bullet}$-PNVO increases to ∼3.2, 5.4, and 8.5 nm when the polymerization temperatures are set as 25, 50, and 80 °C, respectively. According to our previous work, the concentration of oxygen vacancies increases with the thickness of the PEDOT coating.[42] Thus, characterizations of oxygen vacancies are ignored here and electrochemical performance optimization is the focus.

All of the above $Vo^{\bullet\bullet}$-PNVO samples were first tested in Na_2SO_4 solution (0.5 M) as symmetrical electrode supercapacitors, and the loading mass was about 1 mg cm^{-2} (Supporting Information). The results show that $Vo^{\bullet\bullet}$-PNVO with an ∼5.4 nm PEDOT coating synthesized at 50 °C exhibits a larger CV area (Figure S3a), a higher specific capacitance (∼383 F g^{-1} at 0.5 A g^{-1}, Figure 5a and Figure S4a−h) and better rate performance (150 F g^{-1} at 10 A g^{-1}) in comparison to the other samples (Figure S3c). For instance, $Vo^{\bullet\bullet}$-PNVO with an ∼8.5 nm PEDOT layer achieves 140 F g^{-1} at 10 A g^{-1}. EIS measurements and the equivalent circuit were applied to explore the kinetic properties, as shown in Figure 5b Figure S3d. In a typical Nyquist plot, the Z' intercept, semicircle, and the line slope correspond to the internal resistance mostly from electrolyte (R_s), resistance from charge transfer at the interface of the electrode and electrolyte (R_{ct}), and resistance from ion diffusion in materials, respectively. For $Vo^{\bullet\bullet}$-PNVO, the almost same R_s values, decreasing R_{ct} values, and steeper slope suggest that the charge transfer and ion diffusion kinetics are enhanced with a thicker PEDOT coating and more oxygen vacancies. This results from the synergistic combination of oxygen vacancies (providing more void sites and larger channels for faster and easier ion diffusion) and a conductive PEDOT coating (shortening the charge transfer distance and promoting charge transportation).[42] However, excessive oxygen vacancies compromise Faradaic reactions with overconsumption of V^{5+}, and thus the capacitance decreases to 344 F g^{-1}. On consideration that a similar mechanism has been systematically studied in our previous work on $Vo^{\bullet\bullet}$-V_2O_5/PEDOT[42] and that this work focuses on the effects of electrolytes on the electrochemical properties of $Vo^{\bullet\bullet}$-PNVO, the mechanism will not be further discussed here. $Vo^{\bullet\bullet}$-PNVO with an ∼5.4 nm PEDOT coating was chosen as the electrode material in the following explorations.

The storage abilities of tailored $Vo^{\bullet\bullet}$-PNVO in Na^+, Zn^{2+}, and Al^{3+} ions were tested in three aqueous electrolytes, including Na_2SO_4 (0.5 M), $ZnSO_4$ (1 M), and $Al_2(SO_4)_3$ (0.5 M). Na^+, Zn^{2+}, and Al^{3+} were kept at the same concentration. In CV curves of $Vo^{\bullet\bullet}$-PNVO (Figure 5d Figure S5a−f), pseudocapacitive behaviors with nearly rectangular-shaped loops are observed in the three different electrolytes, suggesting reversible, successive, and multiple redox reactions.[48,49] Moreover, the voltammetry area appears larger in the order Al^{3+} < Zn^{2+} < Na^+, indicating an increase in specific capacitance. Consistently, the specific capacitances at 0.5 A g^{-1} obtained from the nearly symmetrical GCD curves (Figure 5e) are 383, 376, and 363 F g^{-1} for Na^+, Zn^{2+}, and Al^{3+} storage, respectively. In a neutral aqueous electrolyte, the possible Faradaic reactions can be described as

$$NVO + xM^{n+} + nxe^- \rightarrow M_xNVO \quad (6)$$

where M^{n+} refers to the electrolyte cation and the maximum capacitance is x = 2 ($V^{5+} \rightarrow V^{3+}$) here. Thus, the specific capacitance is related to the number of cations involved (x) and the corresponding valence (n). Note that, in aqueous solutions, metal ions are usually surrounded by H_2O molecules due to electrostatic interactions. For instance, Na^+ attracts the negative oxygen from water molecules.[51] As shown in Figure 5c, different from the small ionic radius increasing in the order Al^{3+} (0.53 Å) < Zn^{2+} (0.75 Å) < Na^+ (1.02 Å), the corresponding hydrate radius is reported to be much larger and shows the decreasing order Al^{3+} (4.75 Å) > Zn^{2+} (4.30 Å) > Na^+ (3.58 Å)[50] because of stronger interactions between multivalent cations and H_2O molecules.[8,51] As all cations show significant differences in their ionic and hydrate radii and electrons (0.083 Å) are much smaller, hydrate radii instead of

https://doi.org/10.1021/acsami.2c02920
ACS Appl. Mater. Interfaces 2022, 14, 19714−19724

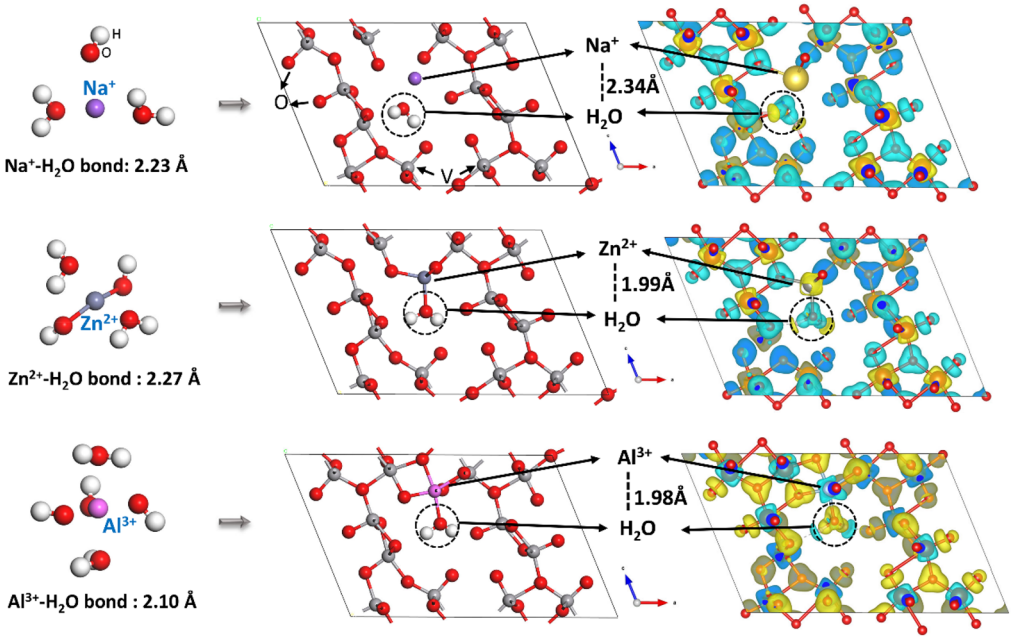

Figure 6. Lengths of M−H_2O bonds (M = Na^+, Zn^{2+}, Al^{3+}) in aqueous solution (left) and in optimized $M_{0.76}V_6O_{15}$ structures and corresponding charge density distributions (right).

multivalent charge carriers should greatly affect the capacitance of $Vo^{\bullet\bullet}$-PNVO. A smaller hydrate radius may show higher mobility and diffusion speed, giving $Vo^{\bullet\bullet}$-PNVO a higher capacitance in Na^+ storage than in Zn^{2+} and Al^{3+} ions. It is also possible that the monovalent Na^+ appears as ions in $Vo^{\bullet\bullet}$-PNVO because of its weaker electrostatic interaction with H_2O in comparison to Zn^{2+} and Al^{3+}, rendering faster Na^+ ion diffusion and higher capacitance in $Vo^{\bullet\bullet}$-PNVO (as evidenced in theoretical calculations).

$Vo^{\bullet\bullet}$-PNVO shows a high specific capacitance at 10 A g^{-1} in Na_2SO_4 (Figure 5f). The specific capacitances in Al^{3+}, Zn^{2+}, and Na^+ electrolytes are 123, 150, and 171 F g^{-1}, respectively, and the corresponding energy densities are 50, 52, and 53 W h g^{-1} at a power density of 250 W kg^{-1}, respectively, better than those of reported vanadium-based supercapacitors[14,43,52,53] (Figure 5g). In addition, $Vo^{\bullet\bullet}$- PNVO exhibits excellent cycling stability, as shown in Figure 5h. About 91% of the initial capacitance is retained in Na_2SO_4 after 20000 charge/discharge cycles, better those in $ZnSO_4$ (86% retention) and $Al_2(SO_4)_3$ (73% retention), as well as reported V_2O_5/PANI nanowires (92% retention after 5000 cycles),[13] a V_2O_5/PPy network (81% retention after 1000 cycles),[54] and MnO_2@PEDOT@MnO_2 (91% retention after 5000 cycles).[55] The corresponding Coulombic efficiency is nearly 100%. Moreover, the capacitance retention is 90% at 1.0 A g^{-1} in Na_2SO_4 after 5000 cycles (Figure S6). SEM and TEM images display that the structure of the cycled $Vo^{\bullet\bullet}$-PNVO electrode is well retained after 20000 cycles in Na_2SO_4 (Figure S7a−c). The reasons can be summarized as follows. First, the excellent stability of $Vo^{\bullet\bullet}$-PNVO is attributed to the PEDOT coating, which protects NVO from contacting electrolyte directly, and also to oxygen vacancies, which offer large diffusion channels for less volume expanse.[35] Moreover, the cycling stability is closely related to the electrolyte cations. In comparison with Zn^{2+} and Al^{3+} hydrates, the smaller Na^+ hydrate radius (or ionic radius) leads to higher insertion/extraction reversibility, resulting in a longer cycling life in Na_2SO_4 solution.

3.3. Kinetic Analysis for Electrochemical Behaviors of Optimized $Vo^{\bullet\bullet}$-PNVO. The interactions between cations and H_2O molecules were identified via density functional theory (DFT in the Supporting Information). On consideration that VASP is limited in calculating the energy of excited states, binding energies (E) of H_2O on Na^+, Zn^{2+}, and Al^{3+} were identified as[29,56]

$$\Delta E = 1/2(E_{M(OH)_n\text{-}2H_2O} - 2E_{H_2O} - E_{M(OH)_n}) \quad (7)$$

where M represents the metal ion, including Na^+, Zn^{2+}, and Al^{3+}, and n = 1, 2, 3 correspond to Na^+, Zn^{2+}, and Al^{3+}, respectively. E_{H_2O}, $E_{M(OH)_n}$, and $E_{M(OH)_n\text{-}2H_2O}$ are the Gibbs free energies of H_2O, $M(OH)_n$, and $M(OH)_n$-$2H_2O$, respectively. The calculation results suggest that all of the three cations coordinate with H_2O molecules as hydrates in aqueous solutions and that Na^+ exhibits a more stable binding energy (−1.00 eV) in comparison to Zn^{2+} (−0.37 eV) and Al^{3+} (−0.69 eV). Note that the calculated binding energy is much smaller than reported values from GAUSSIAN program: for example, about 45−90 kcal mol^{-1} (about 2.6−3.8 eV) for Zn^{2+} coordinated with one to six water molecules.[56] The differences are mainly caused by the limitation of VASP in energy calculations of excited states. However, the overall trend is still comparable because it generally agrees with Gabelich et al.[57] that a monovalent ion which has a small hydrated radius can be more effectively removed from a solution in comparison to a multivalent ion with a large hydrated radius. More importantly, VASP can be used to further explore the states of ion hydrates in the crystal structure in the following part, rather than the GAUSSIAN program.

Water molecules may detach from ion hydrates as ions insert into a crystal structure and have electrostatic interactions with the host structure. Thus, the possibilities of these three ion hydrates in $M_{0.76}V_6O_{15}$ crystal structure were identified, and the optimized structures and charge density differences are shown in Figure 6 and Table 1. In a move from an aqueous solution to $M_{0.76}V_6O_{15}$, the length of the Na^+−H_2O bond

https://doi.org/10.1021/acsami.2c02920
ACS Appl. Mater. Interfaces 2022, 14, 19714−19724

Table 1. Changes in Length of M−H_2O Bonds (M = Na^+, Zn^{2+}, Al^{3+}) in Solution and in the $M_{0.76}V_6O_{15}$ Crystal Structure and the Corresponding Ionic Radii of M

M	length of M−H_2O (Å)		changes in M−H_2O length (Å)	ionic radius of M (Å)
	in solution	in $M_{0.76}V_6O_{15}$		
Na^+	2.23	2.34	+0.11	1.02
Zn^{2+}	2.27	1.99	−0.28	0.75
Al^{3+}	2.10	1.98	−0.12	0.53

shows an increase of 0.11 Å, while Zn^{2+}−H_2O and Al^{3+}−H_2O bonds are reduced by 0.28 and 0.12 Å, respectively. The differences can be explained by, in comparison with divalent Zn^{2+} and trivalent Al^{3+} ions, monovalent Na^+ ions with a larger ionic radius and a single charge have weaker electrostatic interactions with H_2O molecules, and consequently Na^+−H_2O bonds are weaker and Na^+ can be readily unhydrated. No charge transfer between H_2O and Na^+ ions was detected, but it occurred between H_2O and Zn^{2+} or Al^{3+}. The results suggest that Na^+ ions instead of Na^+-H_2O were inserted in $M_{0.76}V_6O_{15}$, whereas Zn^{2+}-H_2O and Al^{3+}-H_2O hydrates were inserted in $M_{0.76}V_6O_{15}$. Consequently, $Vo^{\bullet\bullet}$-PNVO demonstrated a larger capacity and better cycling performance in Na_2SO_4 in comparison to that in both $ZnSO_4$ and $Al_2(SO_4)_3$.

EIS measurements were conducted to study the kinetic behaviors of different cations in tailored $Vo^{\bullet\bullet}$-PNVO (Figure 7a,b). As a result, both R_s and R_{ct} values become larger in the order $R(Na^+) < R(Zn^{2+}) < R(Al^{3+})$, suggesting a smaller resistance in the Na_2SO_4 electrolyte and a faster Na^+ transfer between the electrolyte and the electrode. In addition, the ion diffusion coefficient (D_n) can be obtained by the equation

$$D_n = R^2T^2/(2A^2n^4F^4C^2\sigma^2) \quad (8)$$

where the electrode surface area A, absolute temperature T, Faraday constant F, gas constant R, transferred electron number n, and ion concentration C are constant. The Warburg factor (σ) is obtained by fitting the low-frequency points as Z'' vs $\omega^{-1/2}$ (Figure 7c). As calculated, $Vo^{\bullet\bullet}$-PNVO shows the highest Na^+ diffusion coefficient in the order $D_n(Na^+, 3.2 \times 10^{-10}\ cm^2\ s^{-1}) > D_n(Zn^{2+}, 6.5 \times 10^{-12}\ cm^2\ s^{-1}) > D_n(Al^{3+}, 2.1 \times 10^{-13}\ cm^2\ s^{-1})$, which is also larger than those of $Vo^{\bullet\bullet}$-V_2O_5/PPy ($4.1 \times 10^{-12}\ cm^2\ s^{-1}$), $Vo^{\bullet\bullet}$-V_2O_5/PEDOT ($9.5 \times 10^{-12}\ cm^2\ s^{-1}$), and $Vo^{\bullet\bullet}$-V_2O_5/PANI ($5.2 \times 10^{-12}\ cm^2\ s^{-1}$)[12]. This result agrees well with the above DFT calculations about the formations of Na^+ ions, Zn^{2+}-H_2O, and Al^{3+}-H_2O hydrates in $M_{0.76}V_6O_{15}$. As is illustrated in Figure 7d, Na^+ ions possess a smaller radius in comparison to the Zn^{2+}-H_2O and Al^{3+}-H_2O hydrates and thus show higher mobility and diffuse more quickly than Zn^{2+}-H_2O and Al^{3+}-H_2O hydrates in $Vo^{\bullet\bullet}$-PNVO, givinv $Vo^{\bullet\bullet}$-PNVO a superior electrochemical performance and cycling stability in Na_2SO_4 electrolyte.

4. CONCLUSIONS

Oxygen-deficient $Na_{0.76}V_6O_{15}$/PEDOT ($Vo^{\bullet\bullet}$-PNVO) nanocables with a ∼ 5.4 nm PEDOT coating were tailored as electrode materials for supercapacitors via the synergy of the PEDOT coating and oxygen vacancies. The electrochemical properties and performance of $Vo^{\bullet\bullet}$-PNVO vary significantly with the type of working cations in Na_2SO_4, $ZnSO_4$, and $Al_2(SO_4)_3$ electrolytes. Experimental and DFT results revealed that the three cations exist as hydrates in solutions; however, they are inserted to $Vo^{\bullet\bullet}$-PNVO as Na^+ ions and Zn^{2+}-H_2O and Al^{3+}-H_2O hydrates. Consequently, $Vo^{\bullet\bullet}$-PNVO delivers excellent specific capacitance (383 F g^{-1} at 0.5 A g^{-1}) and long

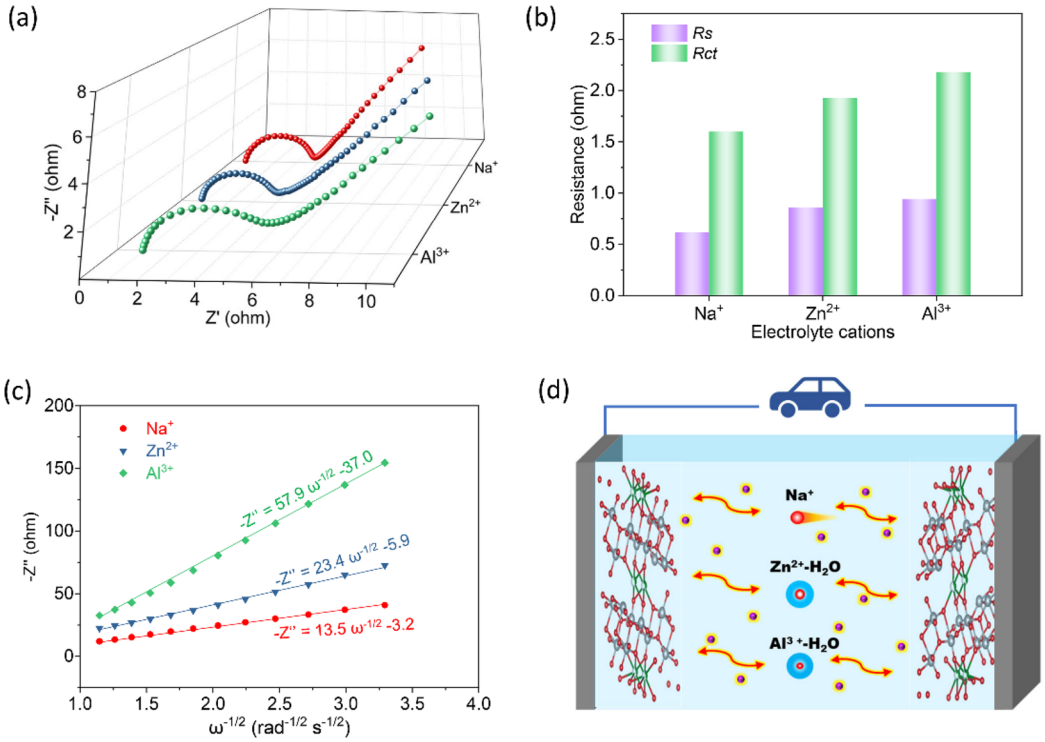

Figure 7. (a) Nyquist plots of $Vo^{\bullet\bullet}$-PNVO in different electrolytes. (b) R_s and R_{ct} of $Vo^{\bullet\bullet}$-PNVO and NVO from their Nyquist plots. (c) Relationship between Z'' and $\omega^{-1/2}$. (d) Schematic diagram of the charge storage mechanism of $Vo^{\bullet\bullet}$-PNVO in different electrolytes.

https://doi.org/10.1021/acsami.2c02920
ACS Appl. Mater. Interfaces 2022, 14, 19714−19724

cycling life (91% capacitance retained over 20000 cycles) in Na_2SO_4 solution, far better than those in both $ZnSO_4$ and $Al_2(SO_4)_3$ electrolytes. This study provides an experimental and theoretical understanding of electrostatic interactions of electrolyte cations for charge storage systems.

■ ASSOCIATED CONTENT

Supporting Information

The Supporting Information is available free of charge at https://pubs.acs.org/doi/10.1021/acsami.2c02920.

TEM-EDS elemental mappings, XRD patterns, CV and GCD curves of $Vo^{\bullet\bullet}$-PNVO, and SEM and TEM images of cycled $Vo^{\bullet\bullet}$-PNVO (PDF)

■ AUTHOR INFORMATION

Corresponding Authors

Guohua Gao − *Shanghai Key Laboratory of Special Artificial Microstructure Materials and Technology, School of Physics Science and Engineering, Tongji University, Shanghai 200092, People's Republic of China;* orcid.org/0000-0002-4233-5357; Email: gao@tongji.edu.cn

Guangming Wu − *Shanghai Key Laboratory of Special Artificial Microstructure Materials and Technology, School of Physics Science and Engineering, Tongji University, Shanghai 200092, People's Republic of China*; Email: wugm@tongji.edu.cn

Guozhong Cao − *Department of Materials Science and Engineering, University of Washington, Seattle, Washington 98195-2120, United States;* orcid.org/0000-0001-6539-0490; Email: gzcao@u.washington.edu

Authors

Wenchao Bi − *Departments of Physics, College of Science, University of Shanghai for Science and Technology, Shanghai 200093, People's Republic of China; Shanghai Key Laboratory of Special Artificial Microstructure Materials and Technology, School of Physics Science and Engineering, Tongji University, Shanghai 200092, People's Republic of China; Department of Materials Science and Engineering, University of Washington, Seattle, Washington 98195-2120, United States*

Xiaodi Jiang − *Shanghai Key Laboratory of Special Artificial Microstructure Materials and Technology, School of Physics Science and Engineering, Tongji University, Shanghai 200092, People's Republic of China*

Chao Li − *Departments of Physics, College of Science, University of Shanghai for Science and Technology, Shanghai 200093, People's Republic of China*

Yuan Liu − *Departments of Physics, College of Science, University of Shanghai for Science and Technology, Shanghai 200093, People's Republic of China*

Muhammad Atif − *Research Chair on Laser Diagnosis of Cancers, Department of Physics and Astronomy, College of Science, King Saud University, 11451 Riyadh, Saudi Arabia; Department of Physics and Astronomy, College of Science, King Saud University, 11451 Riyadh, Saudi Arabia*

Mohamad AlSalhi − *Research Chair on Laser Diagnosis of Cancers, Department of Physics and Astronomy, College of Science, King Saud University, 11451 Riyadh, Saudi Arabia; Department of Physics and Astronomy, College of Science, King Saud University, 11451 Riyadh, Saudi Arabia;* orcid.org/0000-0002-4557-8821

Complete contact information is available at: https://pubs.acs.org/10.1021/acsami.2c02920

Notes

The authors declare no competing financial interest.

■ ACKNOWLEDGMENTS

We are grateful to the National Natural Science Foundation of China (51872204, 22011540379, 52072261), the Shanghai Sailing Program (21YF1430900), the National Key Research and Development Program of China (2017YFA0204600), the Shanghai Social Development Science and Technology Project (20dz1201800), and the National Science Foundation (No. 1803256). We also appreciate the Deanship of Scientific Research at King Saud University for funding through the Vice Deanship of Scientific Research Chairs.

■ REFERENCES

(1) Chu, S.; Majumdar, A. Opportunities and Challenges for A Sustainable Energy Future. *Nature* **2012**, *488* (7411), 294−303.

(2) Gür, T. M. Review of electrical energy storage technologies, materials and systems: challenges and prospects for large-scale grid storage. *Energy Environ. Sci.* **2018**, *11* (10), 2696−2767.

(3) Miller, J. R.; Simon, P. Materials science - Electrochemical capacitors for energy management. *Science* **2008**, *321* (5889), 651−652.

(4) Wang, Y.; Song, Y.; Xia, Y. Electrochemical Capacitors: Mechanism, Materials, Systems, Characterization and Applications. *Chem. Soc. Rev.* **2016**, *45* (21), 5925−5950.

(5) Zhi, M. J.; Xiang, C. C.; Li, J. T.; Li, M.; Wu, N. Q. Nanostructured Carbon-Metal Oxide Composite Electrodes for Supercapacitors: A Review. *Nanoscale* **2013**, *5* (1), 72−88.

(6) Shao, Y.; El-Kady, M. F.; Sun, J.; Li, Y.; Zhang, Q.; Zhu, M.; Wang, H.; Dunn, B.; Kaner, R. B. Design and Mechanisms of Asymmetric Supercapacitors. *Chem. Rev.* **2018**, *118* (18), 9233−9280.

(7) Song, Z.; Zhang, G.; Deng, X.; Zou, K.; Xiao, X.; Momen, R.; Massoudi, A.; Deng, W.; Hu, J.; Hou, H.; Zou, G.; Ji, X. Ultra-Low-Dose Pre-Metallation Strategy Served for Commercial Metal-Ion Capacitors. *Nanomicro Lett.* **2022**, *14* (1), 53.

(8) Reddy, R. N.; Reddy, R. G. Sol-gel MnO2 as an electrode material for electrochemical capacitors. *J. Power Sources* **2003**, *124* (1), 330−337.

(9) Beguin, F.; Presser, V.; Balducci, A.; Frackowiak, E. Carbons and Electrolytes for Advanced Supercapacitors. *Adv. Mater.* **2014**, *26* (14), 2219−2251.

(10) Mendoza-Sánchez, B.; Brousse, T.; Ramirez-Castro, C.; Nicolosi, V.; S. Grant, P. An investigation of nanostructured thin film α-MoO3 based supercapacitor electrodes in an aqueous electrolyte. *Electrochim. Acta* **2013**, *91*, 253−260.

(11) Kim, B.-H.; Kim, C. H.; Yang, K. S.; Rahy, A.; Yang, D. J. Electrospun vanadium pentoxide/carbon nanofiber composites for supercapacitor electrodes. *Electrochim. Acta* **2012**, *83*, 335−340.

(12) Bi, W.; Huang, J.; Wang, M.; Jahrman, E. P.; Seidler, G. T.; Wang, J.; Wu, Y.; Gao, G.; Wu, G.; Cao, G. V_2O_5-Conductive Polymer Nanocables with Built-in Local Electric Field Derived from Interfacial Oxygen Vacancies for High Energy Density Supercapacitors. *J. Mater. Chem. A* **2019**, *7* (30), 17966−17973.

(13) Bai, M. H.; Liu, T. Y.; Luan, F.; Li, Y.; Liu, X.-X. Electrodeposition of Vanadium Oxide-Polyaniline Composite Nanowire Electrodes for High Energy Density Supercapacitors. *J. Mater. Chem. A* **2014**, *2* (28), 10882−10888.

(14) Qu, Q. T.; Shi, Y.; Li, L. L.; Guo, W. L.; Wu, Y. P.; Zhang, H. P.; Guan, S. Y.; Holze, R. V2O5·0.6H2O nanoribbons as cathode material for asymmetric supercapacitor in K2SO4 solution. *Electrochem. Commun.* **2009**, *11* (6), 1325−1328.

(15) Qu, Q. T.; Wang, B.; Yang, L. C.; Shi, Y.; Tian, S.; Wu, Y. P. Study on electrochemical performance of activated carbon in aqueous

Li2SO4, Na2SO4 and K2SO4 electrolytes. *Electrochem. Commun.* **2008**, *10* (10), 1652−1655.
(16) Yang, J.; Xiao, X.; Chen, P.; Zhu, K.; Cheng, K.; Ye, K.; Wang, G.; Cao, D.; Yan, J. Creating oxygen-vacancies in MoO3- nanobelts toward high volumetric energy-density asymmetric supercapacitors with long lifespan. *Nano Energy* **2019**, *58*, 455−465.
(17) Yan, J.; Fan, Z. J.; Wei, T.; Qian, W.; Zhang, M.; Wei, F. Fast and reversible surface redox reaction of graphene-MnO_2 composites as supercapacitor electrodes. *Carbon* **2010**, *48* (13), 3825−3833.
(18) Ghosh, M.; Vijayakumar, V.; Soni, R.; Kurungot, S. A rationally designed self-standing V2O5 electrode for high voltage non-aqueous all-solid-state symmetric (2.0 V) and asymmetric (2.8 V) supercapacitors. *Nanoscale* **2018**, *10* (18), 8741−8751.
(19) Bi, W.; Gao, G.; Wu, Y.; Yang, H.; Wang, J.; Zhang, Y.; Liang, X.; Liu, Y.; Wu, G. Novel Three-Dimensional Island-Chain Structured V_2O_5/Graphene/MWCNT Hybrid Aerogels for Supercapacitors with Ultralong Cycle Life. *RSC Adv.* **2017**, *7* (12), 7179−7187.
(20) Snook, G. A.; Kao, P.; Best, A. S. Conducting-Polymer-Based Supercapacitor Devices and Electrodes. *J. Power Sources* **2011**, *196* (1), 1−12.
(21) Tong, L.; Skorenko, K. H.; Faucett, A. C.; Boyer, S. M.; Liu, J.; Mativetsky, J. M.; Bernier, W. E.; Jones, W. E. Vapor-phase polymerization of poly(3,4ethylenedioxy thiophene) (PEDOT) on commercial carbon coated aluminum foil as enhanced electrodes for supercapacitors. *J. Power Sources* **2015**, *297*, 195−201.
(22) Yan, P.; Zheng, J.; Gu, M.; Xiao, J.; Zhang, J. G.; Wang, C. M. Intragranular Cracking as A Critical Barrier for High-Voltage Usage of Layer-Structured Cathode for Lithium-Ion Batteries. *Nat. Commun.* **2017**, *8*, 14101−14110.
(23) Kim, H. S.; Cook, J. B.; Lin, H.; Ko, J. S.; Tolbert, S. H.; Ozolins, V.; Dunn, B. Oxygen Vacancies Enhance Pseudocapacitive Charge Storage Properties of MoO_{3-x}. *Nat. Mater.* **2017**, *16* (4), 454−460.
(24) Bi, W.; Wang, J.; Jahrman, E. P.; Seidler, G. T.; Gao, G.; Wu, G.; Cao, G. Interface Engineering V_2O_5 Nanofibers for High-Energy and Durable Supercapacitors. *Small* **2019**, *15* (31), 1901747.
(25) Bi, W.; Gao, G.; Wu, G.; Atif, M.; AlSalhi, M. S.; Cao, G. Sodium vanadate/PEDOT nanocables rich with oxygen vacancies for high energy conversion efficiency zinc ion batteries. *Energy Storage Mater.* **2021**, *40*, 209−218.
(26) Kresse, G.; Furthmüller, J. Efficiency of ab-initio total energy calculations for metals and semiconductors using a plane-wave basis set. *Comput. Mater. Sci.* **1996**, *6* (1), 15−50.
(27) Perdew, J. P.; Burke, K.; Ernzerhof, M. Generalized Gradient Approximation Made Simple. *Phys. Rev. Lett.* **1996**, *77* (18), 3865−3868.
(28) Blochl, P. E. Projector augmented-wave method. *Phys. Rev. B: Condens Matter* **1994**, *50* (24), 17953−17979.
(29) Kresse, G.; Joubert, D. From ultrasoft pseudopotentials to the projector augmented-wave method. *Phys. Rev. B* **1999**, *59* (3), 1758−1775.
(30) Mueller, T.; Hautier, G.; Jain, A.; Ceder, G. Evaluation of Tavorite-Structured Cathode Materials for Lithium-Ion Batteries Using High-Throughput Computing. *Chem. Mater.* **2011**, *23* (17), 3854−3862.
(31) Lawal, A. T.; Wallace, G. G. Vapour phase polymerisation of conducting and non-conducting polymers: a review. *Talanta* **2014**, *119*, 133−43.
(32) Liu, C.; Neale, Z.; Zheng, J.; Jia, X.; Huang, J.; Yan, M.; Tian, M.; Wang, M.; Yang, J.; Cao, G. Expanded hydrated vanadate for high-performance aqueous zinc-ion batteries. *Energy Environ. Sci.* **2019**, *12* (7), 2273−2285.
(33) Wang, M.; Zhang, J.; Zhang, L.; Li, J.; Wang, W.; Yang, Z.; Zhang, L.; Wang, Y.; Chen, J.; Huang, Y.; Mitlin, D.; Li, X. Graphene-like Vanadium Oxygen Hydrate (VOH) Nanosheets Intercalated and Exfoliated by Polyaniline (PANI) for Aqueous Zinc-Ion Batteries (ZIBs). *ACS Appl. Mater. Interfaces* **2020**, *12* (28), 31564−31574.
(34) Wu, H.; Yu, G.; Pan, L.; Liu, N.; McDowell, M. T.; Bao, Z.; Cui, Y. Stable Li-ion battery anodes by in-situ polymerization of conducting hydrogel to conformally coat silicon nanoparticles. *Nat. Commun.* **2013**, *4*, 1943.
(35) Bi, W.; Wu, Y.; Liu, C.; Wang, J.; Du, Y.; Gao, G.; Wu, G.; Cao, G. Gradient Oxygen Vacancies in V_2O_5/PEDOT Nanocables for High-Performance Supercapacitors. *ACS Appl. Energy Mater.* **2019**, *2* (1), 668−677.
(36) Zhu, K.; Wu, T.; Huang, K. NaCa0.6V6O16·3H2O as an Ultra-Stable Cathode for Zn-Ion Batteries: The Roles of Pre-Inserted Dual-Cations and Structural Water in V3O8 Layer. *Adv. Energy Mater.* **2019**, *9* (38), 1901968.
(37) Bin, D.; Huo, W.; Yuan, Y.; Huang, J.; Liu, Y.; Zhang, Y.; Dong, F.; Wang, Y.; Xia, Y. Organic-Inorganic-Induced Polymer Intercalation into Layered Composites for Aqueous Zinc-Ion Battery. *Chem.* **2020**, *6* (4), 968−984.
(38) Yang, W.; Dong, L.; Yang, W.; Xu, C.; Shao, G.; Wang, G. 3D Oxygen-Defective Potassium Vanadate/Carbon Nanoribbon Networks as High-Performance Cathodes for Aqueous Zinc-Ion Batteries. *Small Methods* **2020**, *4* (1), 1900670.
(39) Manikandan, R.; Raj, C. J.; Rajesh, M.; Kim, B. C.; Park, S.; Yu, K. H. Vanadium Pentoxide with H2O, K+, and Na+ Spacer between Layered Nanostructures for High-Performance Symmetric Electrochemical Capacitors. *Adv. Mater. Interfaces* **2018**, *5* (12), 1800041.
(40) Xu, D.; Wang, H.; Li, F.; Guan, Z.; Wang, R.; He, B.; Gong, Y.; Hu, X. Conformal Conducting Polymer Shells on V2O5 Nanosheet Arrays as a High-Rate and Stable Zinc-Ion Battery Cathode. *Adv. Mater. Interfaces* **2019**, *6* (2), 1801506−1801514.
(41) Zhao, X.; Dong, M.; Zhang, J.; Li, Y.; Zhang, Q. Vapor-phase polymerization of poly(3, 4-ethylenedioxythiophene) nanofibers on carbon cloth as electrodes for flexible supercapacitors. *Nanotechnology* **2016**, *27* (38), 385705.
(42) Bi, W.; Jahrman, E.; Seidler, G.; Wang, J.; Gao, G.; Wu, G.; Atif, M.; AlSalhi, M.; Cao, G. Tailoring Energy and Power Density through Controlling the Concentration of Oxygen Vacancies in V_2O_5/PEDOT Nanocable-Based Supercapacitors. *ACS Appl. Mater. Interfaces* **2019**, *11* (18), 16647−16655.
(43) Guo, C. X.; Yilmaz, G.; Chen, S.; Chen, S.; Lu, X. Hierarchical Nanocomposite Composed of Layered V_2O_5/PEDOT/MnO_2 Nanosheets for High-performance Asymmetric Supercapacitors. *Nano Energy* **2015**, *12*, 76−87.
(44) Zhang, J.; Yang, H.; Shen, G.; Cheng, P.; Zhang, J.; Guo, S. Reduction of graphene oxide via L-ascorbic acid. *Chem. Commun.* **2010**, *46* (7), 1112−4.
(45) Zeng, Y.; Lai, Z.; Han, Y.; Zhang, H.; Xie, S.; Lu, X. Oxygen-Vacancy and Surface Modulation of Ultrathin Nickel Cobaltite Nanosheets as a High-Energy Cathode for Advanced Zn-Ion Batteries. *Adv. Mater.* **2018**, *30*, 1802396.
(46) Xu, H.; Cheng, C.; Chu, S.; Zhang, X.; Wu, J.; Zhang, L.; Guo, S.; Zhou, H. Anion-Cation Synergetic Contribution to High Capacity, Structurally Stable Cathode Materials for Sodium-Ion Batteries. *Adv. Funct. Mater.* **2020**, *30* (50), 2005164.
(47) Li, Z.; Ren, Y.; Mo, L.; Liu, C.; Hsu, K.; Ding, Y.; Zhang, X.; Li, X.; Hu, L.; Ji, D.; Cao, G. Impacts of Oxygen Vacancies on Zinc Ion Intercalation in VO2. *ACS Nano* **2020**, *14* (5), 5581−5589.
(48) Simon, P.; Gogotsi, Y. Materials for Electrochemical Capacitors. *Nat. Mater.* **2008**, *7* (11), 845−854.
(49) Zheng, K.; Zeng, Y.; Liu, S.; Zeng, C.; Tong, Y.; Zheng, Z.; Zhu, T.; Lu, X. Valence and surface modulated vanadium oxide nanowires as new high-energy and durable negative electrode for flexible asymmetric supercapacitors. *Energy Storage Mater.* **2019**, *22*, 410−417.
(50) Jia, X.; Liu, C.; Neale, Z. G.; Yang, J.; Cao, G. Active Materials for Aqueous Zinc Ion Batteries: Synthesis, Crystal Structure, Morphology, and Electrochemistry. *Chem. Rev.* **2020**, *120* (15), 7795−7866.
(51) Tansel, B.; Sager, J.; Rector, T.; Garland, J.; Strayer, R. F.; Levine, L.; Roberts, M.; Hummerick, M.; Bauer, J. Significance of hydrated radius and hydration shells on ionic permeability during nanofiltration in dead end and cross flow modes. *Sept. Purif. Technol.* **2006**, *51* (1), 40−47.

https://doi.org/10.1021/acsami.2c02920
ACS Appl. Mater. Interfaces 2022, 14, 19714−19724

(52) Bi, W.; Deng, S.; Tang, H.; Liu, Y.; Shen, J.; Gao, G.; Wu, G.; Atif, M.; AlSalhi, M.; Cao, G. Coherent V^{4+} rich V_2O_5/carbon aerogel nanocomposites for high performance supercapacitors. *Sci. China Mater.* **2022**, DOI: 10.1007/s40843-021-1944-9.
(53) Saravanakumar, B.; Purushothaman, K. K.; Muralidharan, G. Interconnected V_2O_5 Nanoporous Network for High-Performance Supercapacitors. *ACS Appl. Mater. Interfaces* **2012**, *4* (9), 4484−4490.
(54) Qian, T.; Xu, N.; Zhou, J. Q.; Yang, T. Z.; Liu, X. J.; Shen, X. W.; Liang, J. Q.; Yan, C. L. Interconnected Three-Dimensional V_2O_5/Polypyrrole Network Nanostructures for High Performance Solid-State Supercapacitors. *J. Mater. Chem. A* **2015**, *3* (2), 488−493.
(55) Tang, P.; Han, L.; Zhang, L.; Wang, S.; Feng, W.; Xu, G.; Zhang, L. Controlled Construction of Hierarchical Nanocomposites Consisting of MnO_2 and PEDOT for High-Performance Supercapacitor Applications. *ChemElectroChem.* **2015**, *2* (7), 949−957.
(56) Bock, C. W.; Katz, A. K.; Glusker, J. P. Hydration of Zinc Ions: A Comparison with Magnesium and Beryllium Ions. *J. Am. Chem. Soc.* **1995**, *117*, 3754−3765.
(57) Gabelich, C. J.; Tran, T. D.; Suffet, I. H. Electrosorption of inorganic salts from aqueous solution using carbon aerogels. *Environ. Sci. Technol.* **2002**, *36* (13), 3010−9.